Research Article Vol. 62, No. 14 / 10 May 2023 / Applied Optics 3703

applied optics

Linear and nonlinear characterization of a broadband integrated Si-rich silicon nitride racetrack ring resonator for on-chip applications

Partha Mondal,[1,2,*] Venkatachalam P.,[1] Radhakant Singh,[1,3] Sneha Shelwade,[1] Gali Sushma,[1] and Shankar K. Selvaraja[1]

[1]Centre for Nano Science and Engineering (CeNSE), Indian Institute of Science, Bangalore, India
[2]Current address: Department of Computer, Electrical and Mathematical Science and Engineering, King Abdullah University of Science and Technology, Thuwal, Saudi Arabia
[3]Current address: AMO GmbH, Otto-Blumenthal-Strasse 25, Aachen 52074, Germany
*parthaphotonica@gmail.com

Received 20 February 2023; revised 9 April 2023; accepted 12 April 2023; posted 14 April 2023; published 4 May 2023

We demonstrate the linear and nonlinear characterization of a plasma-enhanced chemical vapor deposited silicon-rich silicon nitride (SRSN) racetrack ring resonator for on-chip applications within the telecommunication wavelength range. The SRSN waveguide parameters are optimized by employing the refractive index profile measured by ellipsometry to achieve flat dispersion in the telecom band. Furthermore, we measure the thermo-optic coefficient of the micro-resonator by analyzing the temperature-dependent transmission spectra and assess it to be $3.2825 \times 10^{-5}\ °C^{-1}$. Additionally, we study power-dependent transmission spectra to investigate the effect of local heating and nonlinear absorption. The power-dependent transmission spectra exhibit a blueshifting of the resonance peak in the visible and near-IR regions, which indicates the presence of nonlinear losses in that range. The power-dependent transmission spectra almost remain unchanged in the telecom band, revealing the absence of nonlinear losses and excellent thermal stability in that wavelength range. Our experimental results reveal that the SRSN-based structure can be employed potentially to realize linear and nonlinear applications in the telecom band.

https://doi.org/10.1364/AO.488219

1. INTRODUCTION

Over the years, silicon (Si)-photonics has emerged as a promising CMOS-compatible material platform for fabricating low-cost, scalable integrated components for on-chip applications [1,2]. Owing to the high-index contrast, high Kerr coefficient, transparency over a broad wavelength range (telecom to mid-IR), and enhanced device performance, Si-on-insulator (SOI) technologies in Si-photonics has been widely accepted for the future generation of CMOS integrated circuits (ICs). Researchers have harnessed Si-photonics and employed in a plethora of applications, including high-speed data processing, sensing [3,4], nonlinear and quantum photonics [5,6], wavelength-division multiplexing (WDM) systems [7,8], and all-optical signal processing [9]. However, despite the tremendous achievement of Si photonics, the small electronic bandgap of Si (1.12 eV) [6] imposes a fundamental limitation owing to the large two-photon (TPA) and free-carrier absorption (FCA) losses below 2.2 μm wavelength [10]. These nonlinear losses are detrimental to the optical performance even at low power and prevent widespread adoption of the Si platform in the telecommunication band [11–13]. On the other hand, Si exhibits a high thermo-optic coefficient (TOC) ($dn/dt = 1.86 \times 10^{-4}\ K^{-1}$), which makes SOI devices strongly sensitive to the device temperature [14]. The optical properties of Si-based devices are highly influenced by the local heating that arises due to the launch of high-power sources and changes in the environmental temperature. Therefore, Si-based photonic devices face limitations in applications corresponding to high-temperature variation. Different approaches have been reported to reduce the thermal effect of Si-based devices, such as the incorporation of an external metal heater for thermal stabilization [15], cladding layer deposition with a material of negative TOC to compensate for the positive TOC of Si [16,17], and athermal design [18]. The limitation of the Si platform leads to exploring a new flexible CMOS-compatible platform carrying a refractive index lying between Si and SiO_2, which can be realized for a multitude of photonics applications. In the quest for a proper substitution of the Si platform, researchers are harnessing different material platforms to overcome the limitations associated with Si.

Over the years, stoichiometric Si nitride (Si_3N_4) material has gained significant attention as a promising CMOS platform for building photonic ICs (PICs) [19]. Apart from its

CMOS compatibility, it offers multiple advantages, such as a large bandgap with low propagation loss; absence of TPA in the telecom wavelength range; and relatively low TOC ($dn/dt = 2.45 \times 10^{-5}$ K^{-1}) compared to both crystalline and amorphous Si [20]. These fascinating properties of Si_3N_4 are inspiration to employ it in a multitude of applications ranging from nonlinear photonics [21] to high-Q resonators [22] and all-optical signal processing [23]. However, despite many conveniences, Si_3N_4 suffers from potential drawbacks, mainly due to the low-refractive-index contrast between core and cladding layers, which in turn increases the device footprint and also low Kerr nonlinearity.

One of the efficient routes to overcome the bottlenecks is to tailor the optical properties of SiN through proper control over the N/Si ratio of the material [24]. Si-rich Si nitride (SRSN) material has attracted considerable interest due to its fabrication flexibility and the ability to tailor the intrinsic properties between those of Si_3N_4 and Si [25]. By adjusting the ratio of the precursor gases (SiH_4/N_2) in the plasma-enhanced chemical vapor deposited (PECVD) process, the percentage of Si content in the material can be effectively tuned, which provides an effective route to engineer the optical properties of SRSN material [26]. A proper N/Si ratio exhibits optical bandgap variation from 2.7 to 5 eV and refractive indices (n) varying over a wide range from 1.91 to 3.1 at 1550 nm wavelength [27]. On the other hand, the third-order nonlinear coefficient increases effectively with the increase in Si content in the material [28], which has already been demonstrated in a variety of applications such as parametric gain, broadband supercontinuum generation [29], nonlinear signal processing [30,31], and wavelength conversion [32,33]. The TOC as well as the linear and nonlinear refractive indices of SRSN material also increase linearly with the increase in the fractional composition of Si over a range from that of Si_3N_4 to a-Si [27,34]. Hence, careful control over the Si composition in the material is required to realize a thermally stable and high-refractive-index-contrast integrated CMOS SRSN platform.

In this paper, we demonstrate a broadband dispersion-engineered SRSN racetrack ring resonator to realize on-chip applications in the telecommunication band. We design and fabricate grating couplers at the input and output terminals to couple light into the device and perform optical characterizations. We measure the TOC of PECVD SRSN material by determining the temperature-dependent resonance shift of the racetrack ring resonator structure in the transmission spectrum. Furthermore, we investigate the power-dependent transmission spectra to characterize the thermal stability and nonlinear loss in the visible and telecommunication wavelength ranges.

2. DESIGN AND FABRICATION OF SRSN WAVEGUIDE

In the current work, we have employed the PECVD technique using the OXFORD instruments Plasmalab System100 to deposit SRSN onto a Si wafer with a 3 μm thick buried oxide layer. The deposition was done at a low temperature of 350°C and comprises precursor gases NH_3, SiH_4, and N_2 with different flow rates. To characterize the refractive index of SRSN film, we deposit 200 nm of SRSN on the top of a clean Si wafer. After

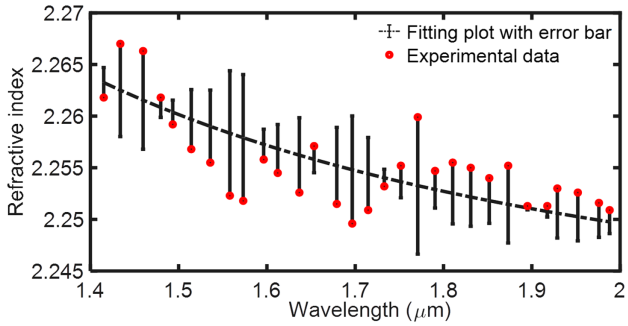

Fig. 1. Refractive index as measured by ellipsometry for the SRSN film and fitting plot following Sellmeier equation with error bar.

that, we carried out ellipsometry measurements with a broad range of wavelengths. Figure 1 shows the dispersion of the real part of the refractive index of the deposited SRSN layer. The fitting plot is carried out with the following Sellmeier equation:

$$n^2_{\mathrm{SRSN}} = 1.4533 + \frac{2.2009\lambda^2}{\lambda^2 - 0.000002^2} + \frac{1.3498\lambda^2}{\lambda^2 - 0.4017^2}, \quad (1)$$

where λ is in the unit of μm. It is observed that the value of the real part of the refractive index is significantly higher than that of Si_3N_4 material, where the deposited SRSN material exhibits a refractive index of 2.258 at 1550 nm. This refractive index profile has been employed for designing the SRSN-based racetrack ring resonator structure.

The waveguide parameters have been optimized using a full-vectorial mode solver to achieve a flat dispersion profile in the telecom wavelength range. The optimized height (H) and width (W) for the SRSN waveguide are 450 and 1000 nm, respectively. Figure 2(a) shows the modal confinement of the fundamental TE mode at 1550 nm for the optimized waveguide parameters. The dispersion profile is shown in Fig. 2(b), which exhibits flat dispersion in the telecom band and can be useful for complex nonlinear applications.

The optimized waveguide parameters have been employed for fabricating the racetrack ring resonator structure. The schematic of the racetrack ring resonator structure is shown in Fig. 4(a). The racetrack resonator is designed for operating in the telecommunication wavelength range. The gap and coupling length have been chosen as 200 nm and 550 μm, respectively. To achieve maximum coupling, the grating coupler has been designed with an SRSN width of 285 nm, shallow-etched depth of 250 nm, and grating period of 870 nm. The coupling efficiency of the optimized design is shown in Fig. 3, which is simulated through Lumerical FDTD software. The 3 dB bandwidth of the grating coupler is calculated as 50 nm. To fabricate the device, we deposit a 3 μm SiO_2 layer on the top of a clean Si wafer by the PECVD method. Furthermore, a 450 nm thick SRSN layer is deposited on the top of the SiO_2 layer employing the PECVD method. The structures are patterned employing a Raith e-LiNE electron-beam lithography system using MaN-2401 as a negative photoresist, followed by reactive ion etching (RIE) with fluorine chemistry. Figure 4(c) shows the microscope view of the fabricated device.

Device characterization is performed using a thermoelectric cooler (TEC)-enabled broadband superluminescent compact laser diode (Thorlabs 1550S-A2), which is connected to

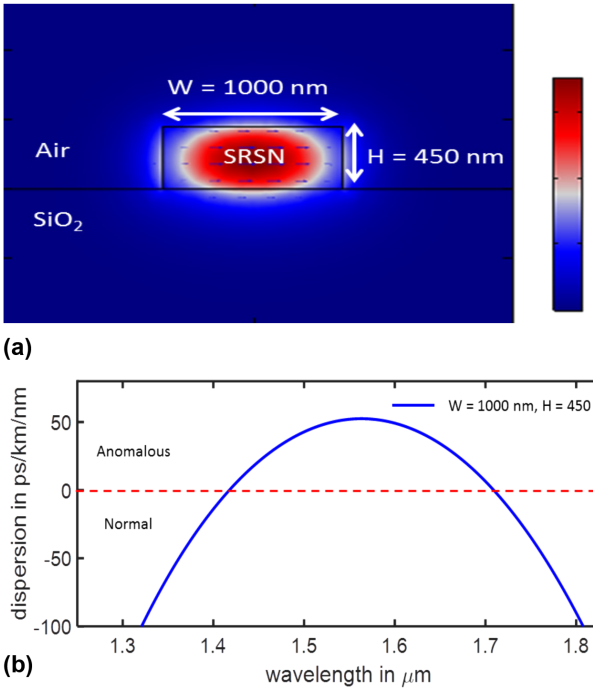

Fig. 2. (a) Schematic of the transverse modal profile of the fundamental TE mode of the proposed waveguide. (b) Dispersion plot of the SRSN waveguide structure.

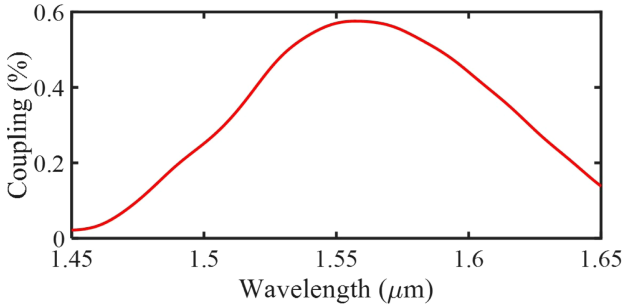

Fig. 3. Simulated coupling efficiency as a function of wavelength.

the input probe with a single-mode fiber passing through a polarization controller and three-axis translation stage. The fiber incident angle is set at 10°. The output signal was collected with an optical spectrum analyzer (OSA) (Yokogawa AQ6370D) ranging from 600 to 1700 nm. Due to the usage of the grating coupler, the coupling efficiency did not change effectively throughout our experiment, and also the laboratory temperature was fixed at 25°C. The normalized TE transmission is shown in Fig. 5. The measured spectrum shows periodic resonance dips with uniform spacing between the adjacent dips. The Q factor measured at 1553.8 nm is 22,500, whereas the full width at half maximum (FWHM) linewidth and free spectral range (FSR) are measured as 0.069 and 0.326 nm, respectively. The racetrack ring resonator structure operates in the critical coupling range, and the propagation loss is measured as 8.5 dB/cm at 1550 nm.

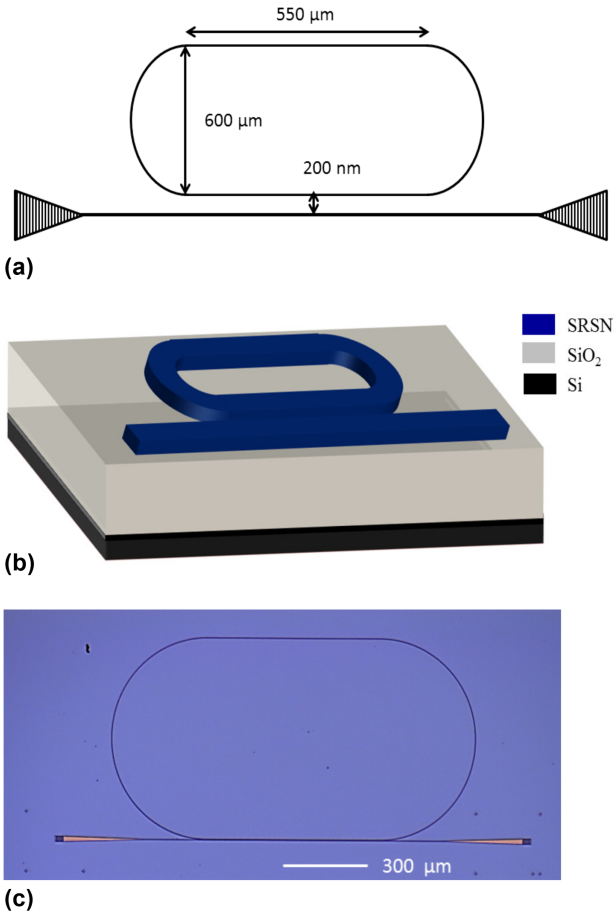

Fig. 4. (a) Schematic diagram of the racetrack ring resonator structure. (b) Perspective view of the racetrack ring resonator and bus waveguide. (c) Optical microscopy image of the racetrack ring resonator along with the bus waveguide and grating coupler.

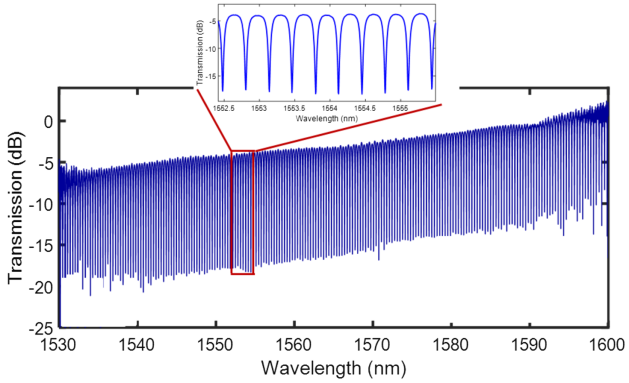

Fig. 5. Measured transmission spectrum of the racetrack ring resonator at the through port for the TE mode.

3. THERMO-OPTIC CHARACTERIZATION

To characterize the thermal response of the device, we have performed temperature-dependent measurements of the SRSN-based racetrack ring resonator platform. Furthermore, we calculate the wavelength shift $\Delta\lambda$ of the resonant peak in the output spectrum with the change in the environmental temperature. The wavelength shift can be calculated as

$$\Delta\lambda = \left(\frac{\partial n_{\text{eff}}}{\partial T_R} + n_{\text{eff}}.\alpha_{\text{sub}}\right)\frac{\lambda}{n_g}\Delta T_R, \tag{2}$$

where λ is the resonance wavelength at room temperature, α_{sub} is the thermal expansion coefficient of the substrate, and ΔT_R is the change in environmental temperature. n_g is the group index, which can be expressed as $n_g = \frac{\lambda^2}{L_R \cdot \text{FSR}}$, L_R and FSR are the resonator length and FSR, respectively. The effective TOC defines the change in the effective index as a function of temperature, which can be expressed as

$$\kappa_{\text{eff}} = \frac{\partial n_{\text{eff}}}{\partial T_R} = \left(\frac{n_g}{\lambda}\frac{\partial \lambda}{\partial T_R} - n_{\text{eff}}.\alpha_{\text{sub}}\right), \tag{3}$$

where $\frac{\partial \lambda}{\partial T_R}$ defines the wavelength shift of the resonance dip as a function of temperature. However, as effective TOC involves modal overlapping between the core of the SRSN waveguide and cladding oxide, Eq. (3) can be rewritten considering the overlapping factor as

$$\kappa_{\text{eff}} = \Gamma_{\text{SiN}_x}\left(\frac{\partial n}{\partial T}\right)_{\text{SiN}_x} + \Gamma_{\text{SiO}_2}\left(\frac{\partial n}{\partial T}\right)_{\text{SiO}_2} + \Gamma_{\text{air}}\left(\frac{\partial n}{\partial T}\right)_{\text{air}}, \tag{4}$$

where Γ_{SiN_x}, Γ_{SiO_2}, and Γ_{air} are the modal overlapping factor with the SRSN waveguide core, cladding oxide, and air, respectively. However, as $\partial n/\partial T$ in air is zero, the last term can be neglected.

The TOC of the platform is determined by using a standard, thermally controlled, passive characterization waveguide setup. The temperature-dependent transmission spectrum for the resonator structure is shown in Fig. 6(a), where the substrate temperature was varied across the range between 40°C and 50°C. The $\partial\lambda/\partial T_R$ value has been calculated by performing a linear fitting of the resonance peak wavelength shifting against the substrate temperature and is shown in Fig. 6(b). The value of $\partial\lambda/\partial T_R$ is obtained as 0.021 nm/°C. Taking L_R and FSR values as 2984 μm and 0.326 nm, respectively, the group index n_g value is calculated as 2.4829. The calculated values of the overlapping factor for Γ_{SiN_x}, Γ_{SiO_2}, and effective mode indices n_{eff} are given by 0.846, 0.096, and 1.854, respectively, which were obtained through the finite difference method. Furthermore, for the calculation, we consider $\alpha_{\text{sub}} = 2.6 \times 10^{-6}$. Putting all these values in Eq. (3), we calculate κ_{eff} as 2.873×10^{-5} °C^{-1}. Considering $(\partial n/\partial T)_{\text{SiO}_2} = 1 \times 10^{-5}$°C^{-1}, TOC of the SRSN waveguide is determined from Eq. (4) to be 3.2825×10^{-5} °C^{-1}. It can be seen that the measured value of TOC is well below that of Si.

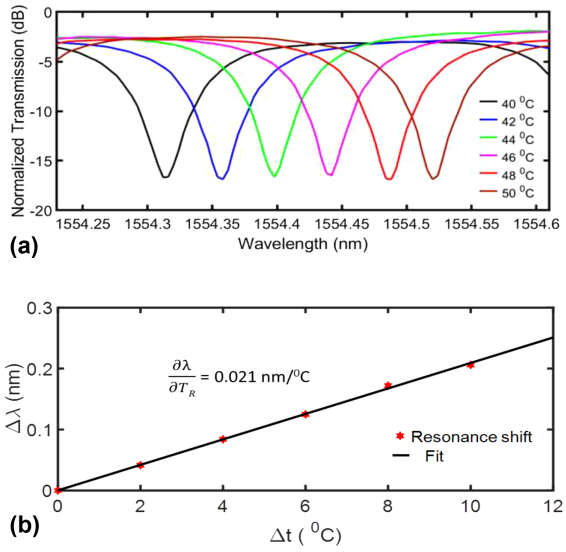

Fig. 6. (a) Spectral response of the resonance dip at different temperatures. (b) Plot of the resonance shift $\Delta\lambda$ as a function of substrate temperature.

4. TPA CHARACTERIZATION

Additionally, to characterize the nonlinear losses, we measure the power-dependent transmission spectrum in both visible and telecommunication regimes. Optical characterization was performed using a tunable laser source and diode laser sources at 528, 780, 1310, and 1550 nm wavelengths. For TPA characterization, the pump source was launched from the top to illuminate the resonator structure. Finally, the output signal was collected by OSA. The transmission spectrum is measured as a function of input optical power. The power-dependent transmission spectrum for the diode laser pumped at 528 nm is shown in Fig. 7(a), where a blueshifted spectral response with an increase in input pump power is observed. The corresponding spectral shift with the incident pump power is shown in Fig. 7(b). The fitting line shows a spectral shift of −3 pm/mW. It is important to note that the direction of the wavelength shifting depends on the dominant nonlinear process. The incident light gets absorbed via TPA, which in turn generates free carriers. The generated free carriers cause the blueshifting of the resonance peaks owing to free carrier dispersion (FCD). On the other hand, the generated free carriers trigger the free carrier absorption (FCA) loss. The combined effect of TPA, FCA, and linear surface absorption leads to heating of the resonator, where the thermo-optic effect causes redshifting of the resonance peak [35,36]. As Si has a high positive TOC, the thermal effect

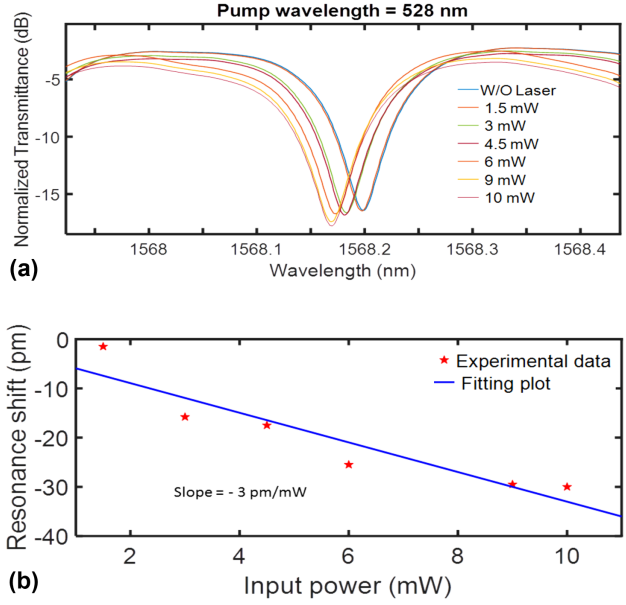

Fig. 7. (a) Power-dependent transmission spectra for diode pump laser at 528 nm and (b) corresponding spectral shift of the resonance wavelength with pump power variation.

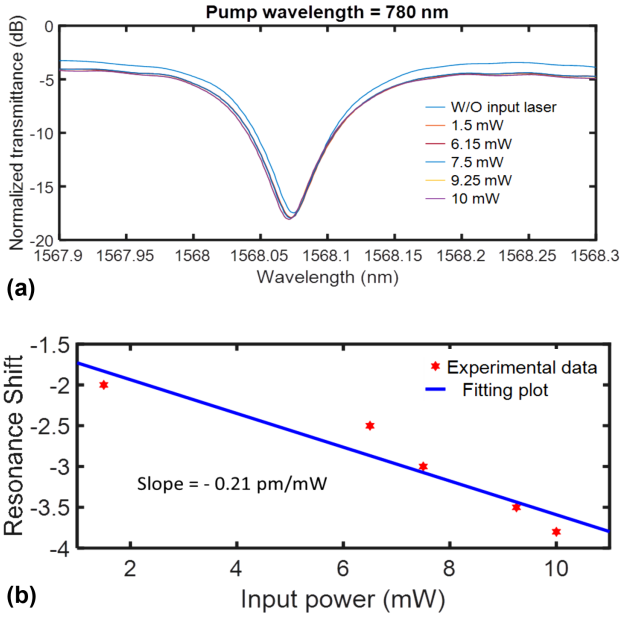

Fig. 8. (a) Power-dependent transmission spectra for diode pump laser at 780 nm and (b) corresponding spectral shift of the resonance wavelength with pump power variation.

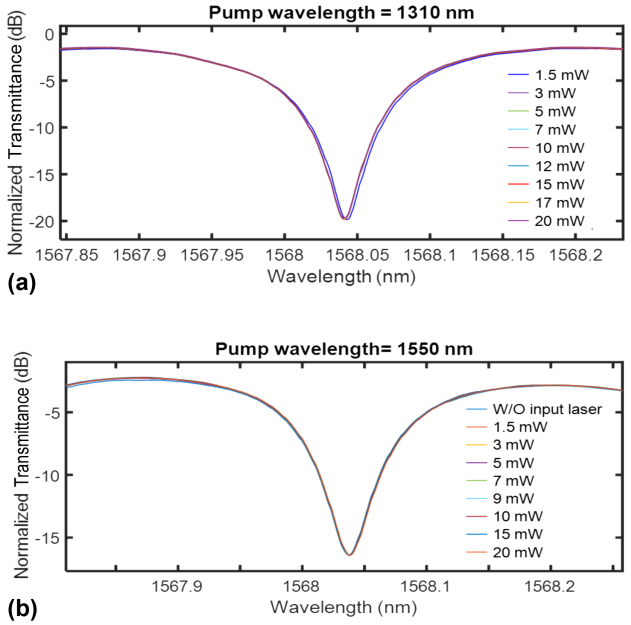

Fig. 9. Power-dependent transmission spectra for diode pump laser at (a) 1310 nm and (b) 1550 nm wavelength.

dominates and exhibits redshifting in Si-based devices [37,38]. In contrast, in our case, we observe a blueshifting of the resonance peak. This is because the SRSN has a much lower TOC as measured in the previous section compared to Si. Hence, the FCD mechanism dominates the thermo-optic effect, resulting in the blueshifting of the spectral peaks. Figure 8(a) exhibits power-dependent transmission spectra for the pump wavelength at 780 nm. A small spectral blueshift is observed at that wavelength. The variation of the resonance shift with the input pump power is shown in Fig. 8(b). The fitting line of the resonance shift exhibits a spectral shift of −0.21 pm/ mW at the wavelength of 780 nm wavelength, which is much lower than that observed at 580 nm. This is because the TPA effect gets reduced at 780 nm wavelength compared to 528 nm. The power-dependent transmission spectrum for a diode laser pumped at 1310 nm is shown in Fig. 9(a). The input power of the diode laser varied from 1.5 to 20 mW. It is observed that the SRSN-based device exhibits efficient thermal stability and suffers from no nonlinear losses as the resonance shape remains almost unchanged. On the other hand, the power-dependent transmission spectrum for a diode laser at 1550 nm is shown in Fig. 9(b), which also exhibits remarkable thermal stability and the absence of nonlinear losses. Variation of the spectral response at different pump wavelengths can be well explained by considering the changes in bandgap with varying Si/N ratios. Table 1 comprises a comparison of the optical properties of Si and SRSN material with varying Si and N composites in the telecom band. As the refractive index increases with the increasing Si content, the bandgap decreases gradually [24]. As a result, the limiting wavelength of the TPA loss decreases. Our results indicate that the SRSN device offers extensive thermal stability and the nonexistence of nonlinear losses in the telecommunication band.

Table 1. Optical Properties of SRSN Material in Comparison with Other Materials

Material	Refractive Index at 1550 nm	TOC $\times 10^{-5}$	β_{TPA} cm/GW
a-Si [24,39,40]	3.73	23	0.25
c-Si [24,39,41]	3.45	18.6	0.45
Si_3N_4 [20]	1.977	2.45	Nil
Si_7N_3 [25,27]	3.1	16.5	0 (>1.2 μm)
SRSN (our work)	2.258	3.2825	Nil

5. CONCLUSION

In conclusion, we have demonstrated an SRSN-based broadband integrated racetrack ring resonator for on-chip applications. SRSN material exhibits an enhanced refractive index of 2.258 at 1550 nm. The TOC of the SRSN platform is characterized by measuring the temperature-dependent transmission spectra for the resonator structure, and the TOC is estimated to be $3.2825 \times 10^{-5°}C^{-1}$. Furthermore, we have measured the power-dependent transmission spectra for different pumping wavelengths ranging from visible to communication band. Transmission spectra almost remain invariant with varying input powers for pumping at the telecom band, which reveals significant thermal stability, and the absence of nonlinear absorption in that band.

Funding. Ministry of Education, India.

Acknowledgment. We acknowledge the Ministry of Electronics and Information Technology for support through the Center of excellence in quantum technology. We also acknowledge funding from the Ministry of Education, Government of India, for supporting facilities at the Centre for Nanoscience and Engineering (CeNSE), Indian Institute of Science, Bangalore.

Disclosures. The authors declare no conflicts of interest.

Data availability. Data underlying the results presented in this paper are not publicly available at this time but may be obtained from the authors upon reasonable request.

REFERENCES

1. R. Soref, "The past, present, and future of silicon photonics," IEEE J. Sel. Top. Quantum Electron. **12**, 1678–1687 (2006).
2. D. Thomson, A. Zilkie, J. E. Bowers, T. Komljenovic, G. T. Reed, L. Vivien, D. Marris-Morini, E. Cassan, L. Virot, J.-M. Fédéli, J.-M. Hartmann, J. H. Schmid, D.-X. Xu, F. Boeuf, P. O'Brien, G. Z. Mashanovich, and M. Nedeljkovic, "Roadmap on silicon photonics," J. Opt. **18**, 073003 (2016).
3. C. Rogers, A. Y. Piggott, D. J. Thomson, R. F. Wiser, I. E. Opris, S. A. Fortune, A. J. Compston, A. Gondarenko, F. Meng, X. Chen, G. T. Reed, and R. Nicolaescu, "A universal 3D imaging sensor on a silicon photonics platform," Nature **590**, 256–261 (2021).
4. D. Dorfner, T. Hürlimann, T. Zabel, L. H. Frandsen, G. Abstreiter, and J. Finley, "Silicon photonic crystal nanostructures for refractive index sensing," Appl. Phys. Lett. **93**, 181103 (2008).
5. N. C. Harris, D. Bunandar, M. Pant, G. R. Steinbrecher, J. Mower, M. Prabhu, T. Baehr-Jones, M. Hochberg, and D. Englund, "Large-scale quantum photonic circuits in silicon," Nanophotonics **5**, 456–468 (2016).
6. J. Leuthold, C. Koos, and W. Freude, "Nonlinear silicon photonics," Nat. Photonics **4**, 535–544 (2010).
7. Q. Fang, T.-Y. Liow, J. F. Song, K. W. Ang, M. B. Yu, G. Q. Lo, and D.-L. Kwong, "WDM multi-channel silicon photonic receiver with 320 gbps data transmission capability," Opt. Express **18**, 5106–5113 (2010).
8. A. Moscoso-Mártir, A. Tabatabaei-Mashayekh, J. Müller, J. Nojić, R. Setter, M. Nielsen, A. Sandomirsky, S. Rockman, E. Mentovich, F. Merget, A. Garreau, F. Lelarge, and J. Witzens, "8-channel WDM silicon photonics transceiver with soa and semiconductor mode-locked laser," Opt. Express **26**, 25446–25459 (2018).
9. C. Koos, L. Jacome, C. Poulton, J. Leuthold, and W. Freude, "Nonlinear silicon-on-insulator waveguides for all-optical signal processing," Opt. Express **15**, 5976–5990 (2007).
10. L. Yin, Q. Lin, and G. P. Agrawal, "Soliton fission and supercontinuum generation in silicon waveguides," Opt. Lett. **32**, 391–393 (2007).
11. L. Yin and G. P. Agrawal, "Impact of two-photon absorption on self-phase modulation in silicon waveguides," Opt. Lett. **32**, 2031–2033 (2007).
12. H. K. Tsang, C. S. Wong, T. K. Liang, I. Day, S. Roberts, A. Harpin, J. Drake, and M. Asghari, "Optical dispersion, two-photon absorption and self-phase modulation in silicon waveguides at 1.5 μm wavelength," Appl. Phys. Lett. **80**, 416–418 (2002).
13. R. Haldar, A. Roy, P. Mondal, V. Mishra, and S. K. Varshney, "Free-carrier-driven Kerr frequency comb in optical microcavities: steady state, bistability, self-pulsation, and modulation instability," Phys. Rev. A **99**, 033848 (2019).
14. P. Dong, W. Qian, H. Liang, R. Shafiiha, N.-N. Feng, D. Feng, X. Zheng, A. V. Krishnamoorthy, and M. Asghari, "Low power and compact reconfigurable multiplexing devices based on silicon microring resonators," Opt. Express **18**, 9852–9858 (2010).
15. S. Manipatruni, R. K. Dokania, B. Schmidt, N. Sherwood-Droz, C. B. Poitras, A. B. Apsel, and M. Lipson, "Wide temperature range operation of micrometer-scale silicon electro-optic modulators," Opt. Lett. **33**, 2185–2187 (2008).
16. M. Han and A. Wang, "Temperature compensation of optical microresonators using a surface layer with negative thermo-optic coefficient," Opt. Lett. **32**, 1800–1802 (2007).
17. F. Qiu, A. M. Spring, H. Miura, D. Maeda, M.-A. Ozawa, K. Odoi, and S. Yokoyama, "Athermal hybrid silicon/polymer ring resonator electro-optic modulator," ACS Photon. **3**, 780–783 (2016).
18. J. Teng, P. Dumon, W. Bogaerts, H. Zhang, X. Jian, X. Han, M. Zhao, G. Morthier, and R. Baets, "Athermal silicon-on-insulator ring resonators by overlaying a polymer cladding on narrowed waveguides," Opt. Express **17**, 14627–14633 (2009).
19. D. J. Moss, R. Morandotti, A. L. Gaeta, and M. Lipson, "New cmos-compatible platforms based on silicon nitride and hydex for nonlinear optics," Nat. Photonics **7**, 597–607 (2013).
20. A. Arbabi and L. L. Goddard, "Measurements of the refractive indices and thermo-optic coefficients of Si3N4 and SiOx using microring resonances," Opt. Lett. **38**, 3878–3881 (2013).
21. M. H. Pfeiffer, C. Herkommer, J. Liu, H. Guo, M. Karpov, E. Lucas, M. Zervas, and T. J. Kippenberg, "Octave-spanning dissipative Kerr soliton frequency combs in Si3N4 microresonators," Optica **4**, 684–691 (2017).
22. K. Luke, Y. Okawachi, M. R. Lamont, A. L. Gaeta, and M. Lipson, "Broadband mid-infrared frequency comb generation in a Si3N4 microresonator," Opt. Lett. **40**, 4823–4826 (2015).
23. T. Sharma, J. Wang, B. K. Kaushik, Z. Cheng, R. Kumar, Z. Wei, and X. Li, "Review of recent progress on silicon nitride-based photonic integrated circuits," IEEE Access **8**, 195436–195446 (2020).
24. D. Tan, K. Ooi, and D. Ng, "Nonlinear optics on silicon-rich nitride—a high nonlinear figure of merit cmos platform," Photon. Res. **6**, B50–B66 (2018).
25. B.-U. Sohn, J. W. Choi, D. K. Ng, and D. T. Tan, "Optical nonlinearities in ultra-silicon-rich nitride characterized using z-scan measurements," Sci. Rep. **9**, 1–7 (2019).
26. D. T. Tan, D. Ng, J. Choi, E. Sahin, B.-U. Sohn, G. Chen, P. Xing, H. Gao, and Y. Cao, "Nonlinear optics in ultra-silicon-rich nitride devices: recent developments and future outlook," Adv. Phys.: X **6**, 1905544 (2021).
27. H. Nejadriahi, A. Friedman, R. Sharma, S. Pappert, Y. Fainman, and P. Yu, "Thermo-optic properties of silicon-rich silicon nitride for on-chip applications," Opt. Express **28**, 24951–24960 (2020).
28. C. J. Krückel, A. Fülöp, T. Klintberg, J. Bengtsson, P. A. Andrekson, and V. Torres-Company, "Linear and nonlinear characterization of low-stress high-confinement silicon-rich nitride waveguides," Opt. Express **23**, 25827–25837 (2015).
29. X. Liu, M. Pu, B. Zhou, C. J. Krückel, A. Fülöp, V. Torres-Company, and M. Bache, "Octave-spanning supercontinuum generation in a silicon-rich nitride waveguide," Opt. Lett. **41**, 2719–2722 (2016).
30. M. R. Dizaji, C. J. Krückel, A. Fülöp, P. A. Andrekson, V. Torres-Company, and L. R. Chen, "Silicon-rich nitride waveguides for ultra-broadband nonlinear signal processing," Opt. Express **25**, 12100–12108 (2017).
31. C. Lacava, S. Stankovic, A. Z. Khokhar, T. D. Bucio, F. Gardes, G. T. Reed, D. J. Richardson, and P. Petropoulos, "Si-rich silicon nitride for nonlinear signal processing applications," Sci. Rep. **7**, 1–13 (2017).
32. M. Yang, L. Xu, J. Wang, H. Liu, X. Zhou, G. Li, and L. Zhang, "An octave-spanning optical parametric amplifier based on a low-dispersion silicon-rich nitride waveguide," IEEE J. Sel. Top. Quantum Electron. **24**, 1–7 (2018).
33. C. Lacava, T. D. Bucio, A. Khokhar, P. Horak, Y. Jung, F. Gardes, D. Richardson, P. Petropoulos, and F. Parmigiani, "Intermodal frequency generation in silicon-rich silicon nitride waveguides," Photon. Res. **7**, 615–621 (2019).
34. N. G. Pruiti, C. Klitis, C. Gough, S. May, and M. Sorel, "Thermo-optic coefficient of pecvd silicon-rich silicon nitride," Opt. Lett. **45**, 6242–6245 (2020).
35. L.-W. Luo, G. S. Wiederhecker, K. Preston, and M. Lipson, "Power insensitive silicon microring resonators," Opt. Lett. **37**, 590–592 (2012).
36. Y. Gao, W. Zhou, X. Sun, H. K. Tsang, and C. Shu, "Cavity-enhanced thermo-optic bistability and hysteresis in a graphene-on-Si3N4 ring resonator," Opt. Lett. **42**, 1950–1953 (2017).
37. V. Jeyaselvan and S. K. Selvaraja, "Mitigation of carrier induced optical bistability in silicon ring resonators," Opt. Commun. **493**, 127021 (2021).
38. C. Xiang, W. Jin, J. Guo, C. Williams, A. M. Netherton, L. Chang, P. A. Morton, and J. E. Bowers, "Effects of nonlinear loss in high-Q Si ring resonators for narrow-linewidth III-V/Si heterogeneously integrated tunable lasers," Opt. Express **28**, 19926–19936 (2020).
39. M. De Dood, A. Polman, T. Zijlstra, and E. Van der Drift, "Amorphous silicon waveguides for microphotonics," J. Appl. Phys. **92**, 649–653 (2002).

40. F. G. Della Corte, M. E. Montefusco, L. Moretti, I. Rendina, and A. Rubino, "Study of the thermo-optic effect in hydrogenated amorphous silicon and hydrogenated amorphous silicon carbide between 300 and 500 k at 1.55 μm," Appl. Phys. Lett. **79**, 168–170 (2001).

41. G. Cocorullo, F. Della Corte, and I. Rendina, "Temperature dependence of the thermo-optic coefficient in crystalline silicon between room temperature and 550 K at the wavelength of 1523 nm," Appl. Phys. Lett. **74**, 3338–3340 (1999).